An Improved Wavefront Control Algorithm for Large Space Telescopes

Erkin Sidick*, Scott A. Basinger, and David C. Redding
Jet Propulsion Laboratory, California Institute of Technology, 4800 Oak Grove Drive, Pasadena, CA, USA 91109

ABSTRACT

Wavefront sensing and control is required throughout the mission lifecycle of large space telescopes such as James Webb Space Telescope (JWST). When an optic of such a telescope is controlled with both surface-deforming and rigid-body actuators, the sensitivity-matrix obtained from the exit pupil wavefront vector divided by the corresponding actuator command value can sometimes become singular due to difference in actuator types and in actuator command values. In this paper, we propose a simple approach for preventing a sensitivity-matrix from singularity. We also introduce a new "minimum-wavefront and optimal control compensator". It uses an optimal control gain matrix obtained by feeding back the actuator commands along with the measured or estimated wavefront phase information to the estimator, thus eliminating the actuator modes that are not observable in the wavefront sensing process.

Keywords: Wave-front sensing and control, adaptive optics, deformable mirrors, space telescopes.

1. INTRODUCTION

Wavefront sensing and control (WFS&C) is required throughout the mission lifecycle of large space telescopes such as JWST [1]. The most commonly used control technique is the "minimum-wavefront" compensator. In this approach, the wavefront is computed at the exit pupil and is used to determine new actuator commands for the controllable optics using a linear matrix model of the optics. The matrices defining a system are either obtained theoretically from modeling or measured directly from the optics. The telescope typically uses a combination of two kinds of actuators: Surface-deforming (SD) actuators and rigid-body (RB) actuators. The former is used to control the surface shape of a deformable mirror, and the latter is used to move a controllable optic in up to 6 degrees of freedom, including translations and rotations.

The control input for SD actuators are usually tracked either in voltage or in stroke, and the inputs for RB degrees of freedom can be bookkept as rotations and translations of the optic. In the linear matrix model, the normalized influence functions are obtained, which measure the change in the wavefront, ray-by-ray, by applying control degrees of freedom one at a time, and dividing the change in wavefront by the magnitude of the actuation. These influence functions are equivalent to an optical sensitivity matrix whose pseudo-inverse is the least-squares control gain-matrix. However, the sensitivity and the gain matrices can easily become ill-conditioned because of the vast differences in control input parameters. In such a case, the WFC process becomes either numerically unstable or operationally inefficient. In this paper, we propose a method to overcome this problem. We show that by using a set of appropriately chosen scaling factors for actuator commands and optimizing the number of eigenmodes or the threshold of the singular values retained, one can achieve high numerical stability and high operational efficiency in the WFC of large space optics. We also introduce two new compensators. One is "minimum-wavefront and optimal control compensator", and the other is its spatially-filtered and generalized version. In these approaches, the cost function to be minimized is the squared-sum of the wavefront phase error values plus the squared-sum of actuator commands. This is equivalent to feeding back the actuator commands along with the measured wavefront phase information to the estimator, and in the compensator, using the optimal control gains that do not actuate unobservable actuator modes. Such an approach eliminates the actuator modes that are not observable in the wavefront sensing process. Some aspects of this approach have been described in the control law of a Shack-Hartmann sensor based adaptive optics system for the Palomar Mountain Hale Telescope [2]. Here we consider only an interferometric-based WFS system, and will present the new methods along with modeling and simulation results.

*Erkin.Sidick@jpl.nasa.gov; Phone 1 818 393-7585; Fax 1 818 393-9471; www.jpl.nasa.gov

Adaptive Optics Systems, edited by Norbert Hubin, Claire E. Max, Peter L. Wizinowich,
Proc. of SPIE Vol. 7015, 70154P, (2008)
0277-786X/08/$18 · doi: 10.1117/12.786679

2. BRIEF DESCRIPTION OF THE OPITCAL SYSTEM

This paper is not about a particular space telescope. However, to explain our method for improving the sensitivity matrix and our new compensators, we will show some numerical examples. The optical system used to generate our simulation results is based on the High-Contrast Imaging Testbed (HCIT) at Jet Propulsion Laboratory (JPL), California Institute of Technology [3-4]. In this section, we briefly describe the HCIT's optical system. The schematic diagram of the HCIT layout in the *xz*-plane is shown in Figure 1. Artificial starlight is created by a 5μm pinhole illuminated by an optical fiber. An off-axis parabolic mirror (OAP1) collimates the light from the pinhole and directs it to a high-density, 32x32 actuator deformable mirror (DM), which performs wavefront control. A circular aperture mask on the DM defines the system pupil of the HCIT, and has a diameter of D=30mm. After the DM, the collimated light is re-imaged onto the focal plane of an occulting mask by OAP2 and a fold-mirror (FM1). An occulting mask attenuates the starlight, and almost has no effect on off-axis light, potentially reflected from an orbiting planet. The "back-end" of the system, from the occulting mask to the back focus plane, supports experimentation with diverse coronagraph configurations and apodizations. A fold-mirror (FM2) and OAP3 re-collimate the light passing through the occulter mask and form a same-size sharp image of the DM pupil at the Lyot plane. A Lyot Stop blocks the ring-like residual light diffracted off the occulting mask while letting most of the off-axis planet light through. After OAP4 forms an image from the remaining stellar and planet lights, it is then magnified (M≈3) by the OPA5-OAP6 pair for proper sampling on the CCD science camera located at the back focal plane. More information on the HCIT and the DM can be found in Refs. [3-4]. In the present case, we use this system as a standard imaging system without including the Occulter Mask and the Lyot Stop in our optical model. The assumed wavelength of the illuminating beam in our numerical simulations is λ = 785nm.

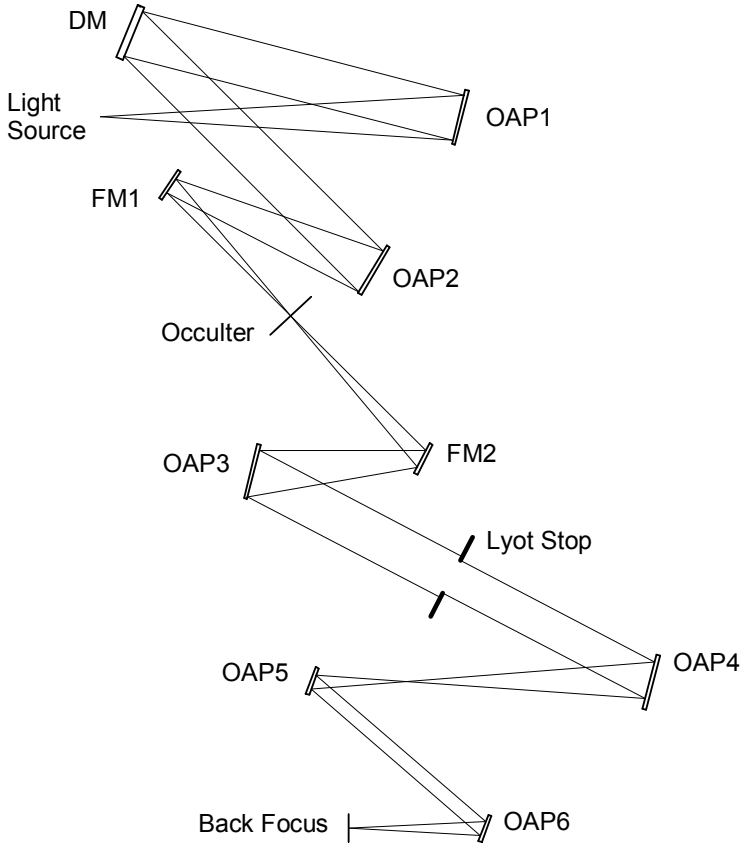

Figure 1. Schematic diagram of the High Contrast Imaging Testbed layout. The light source ("starlight") is a 5μm pinhole illuminated by an optical fiber, and a CCD science camera is located at the back focal plane for detecting the image of the "starlight".

3. MATHEMATICAL NOTATIONS

The wavefront phase error at the exit pupil of an optical system can be represented by a 2D, $m_{\mathrm{w}} \times n_{\mathrm{w}}$ matrix which we denote as $\widetilde{\mathbf{W}}$. In the formulations that follows, we also use a wavefront phase column-vector, notated as $\vec{\mathbf{w}}$. $\vec{\mathbf{w}}$ is formed by stacking the elements of $\widetilde{\mathbf{W}}$ falling inside the exit pupil clear aperture in a certain order, see the following pair as an example:

$$\widetilde{\mathbf{W}} = \begin{bmatrix} 0 & 0 & 5 & 0 & 0 \\ 0 & 2 & 6 & 10 & 0 \\ 1 & 3 & 7 & 11 & 13 \\ 0 & 4 & 8 & 12 & 0 \\ 0 & 0 & 9 & 0 & 0 \end{bmatrix}, \quad \vec{\mathbf{w}}^T = \begin{bmatrix} 1 & 2 & 3 & 4 & 5 & 6 & 7 & 8 & 9 & 10 & 11 & 12 & 13 \end{bmatrix}, \tag{1}$$

where the superscript "*T*" denotes a matrix-transpose. The zero values within $\widetilde{\mathbf{W}}$ represent the gridded data points outside the clear aperture of the exit pupil, and hence are not necessary for computations regarding the wavefront.

The sensitivity vector $\vec{\mathbf{s}}_i$ (also called "Influence Function") of the *i*th degree of freedom (DOF) is defined as the difference of the nominal wavefront and the wavefront resulting from a displacement of the *i*th DOF, represented by vectors, $\vec{\mathbf{w}}_0$ and $\vec{\mathbf{w}}_i$, divided by the magnitude of the displacement, u_i. That is,

$$\vec{\mathbf{s}}_i = \frac{\vec{\mathbf{w}}_i - \vec{\mathbf{w}}_0}{u_i}. \tag{2}$$

$\vec{\mathbf{s}}_i$ is computed for each controllable DOF in the system through numerical differentiation, by recording the initial wavefront $\vec{\mathbf{w}}_0$, and then displacing individual DOFs one at a time and recording the new $\vec{\mathbf{w}}_i$. This can be done using the model or measured directly with an interferometer. The corresponding sensitivity-matrix for all *N* actuators is

$$\widetilde{\mathbf{S}} = \begin{bmatrix} \vec{\mathbf{s}}_1 & \vec{\mathbf{s}}_2 & \ldots & \vec{\mathbf{s}}_{N_{\mathrm{a}}} \end{bmatrix}, \tag{3}$$

where N_{a} is the total number of DOFs. In general, $\widetilde{\mathbf{S}}$ has two parts: The first N_{sda} columns correspond to the SD actuators, and its last N_{rba} columns correspond to the RB actuators, where the subscripts "sda" and "rba" stand for "surface-deforming actuator" and "rigid-body actuator", respectively. That is,

$$\widetilde{\mathbf{S}} = \begin{bmatrix} \widetilde{\mathbf{S}}_{\mathrm{sda}} & \widetilde{\mathbf{S}}_{\mathrm{rba}} \end{bmatrix}. \tag{4}$$

Thus, $N_{\mathrm{a}} = N_{\mathrm{sda}} + N_{\mathrm{rba}}$ and $\widetilde{\mathbf{S}}$ is a $N_{\mathrm{w}} \times N_{\mathrm{a}}$ matrix. In general, $\vec{\mathbf{w}}_0$ includes the nominal wavefront $\vec{\mathbf{w}}_{\mathrm{nom}}$ present by design when the telescope is unaberrated, the wavefront $\vec{\mathbf{w}}_{\mathrm{abr}}$ caused by aberrations to the system, and the wavefront $\vec{\mathbf{w}}_{\mathrm{u}}$ produced by applying a set of actuator commands. That is,

$$\vec{\mathbf{w}}_0 = \vec{\mathbf{w}}_{\mathrm{nom}} + \vec{\mathbf{w}}_{\mathrm{abr}} + \vec{\mathbf{w}}_{\mathrm{u}}. \tag{5}$$

$\vec{\mathbf{w}}_0$ can be obtained by setting the commands of all actuators to zero ($\vec{\mathbf{w}}_{\mathrm{u}}$ =0), or with a set of $\vec{\mathbf{u}}_0$ to achieve a desired state of the telescope. The nominal wavefront $\vec{\mathbf{w}}_{\mathrm{nom}}$ is not usually zero, but rather has some small astigmatism as a result of balancing aberrations among various optics to meet the field performance objectives of the telescope.

A full cycle WFC process includes the following steps:

(1) Apply a set of actuator commands, $\vec{\mathbf{u}}_0$, and measure or estimate the combined initial wavefront, $\vec{\mathbf{w}}_0$. For small motions of the actuators, $\vec{\mathbf{w}}_u$ is a linear function of $\vec{\mathbf{u}}_0$. Therefore, this can be expressed mathematically as

$$\vec{\mathbf{w}}_u = \widetilde{\mathbf{S}}\vec{\mathbf{u}}_0 . \tag{6}$$

"Small" refers to the range of perturbations over which the small-angle approximation is valid for a ray-trace through the optical system.

(2) Generate a new set of actuator commands based on $\vec{\mathbf{w}}_0$. In its simplest form, our control objective is to select the differential commands $\Delta\vec{\mathbf{u}}$ such that they will drive the post-control WF error (WFE),

$$\vec{\mathbf{w}}_\mathrm{f} = \vec{\mathbf{w}}_0 + \widetilde{\mathbf{S}}\Delta\vec{\mathbf{u}} , \tag{7}$$

to its minimum. That is, $\vec{\mathbf{w}}_\mathrm{f}$ is the wavefront after one WFC cycle. One can achieve this by minimizing the cost function *J*:

$$J = \frac{1}{2}\sum_{k=1}^{N_\mathrm{w}} {w_{\mathrm{f}k}}^2 , \tag{8}$$

In matrix form, this becomes

$$J = \frac{1}{2}{\vec{\mathbf{w}}_\mathrm{f}}^T \vec{\mathbf{w}}_\mathrm{f} . \tag{9}$$

If we take the derivative of *J* with respect to the actuator commands, the optimal solution occurs when d*J* is zero, that is,

$$dJ \approx \sum_{i=1}^{N_\mathrm{a}} \left(\frac{\partial {\vec{\mathbf{w}}_\mathrm{f}}^T}{\partial u_i} \Delta u_i \right) \vec{\mathbf{w}}_\mathrm{f} = \Delta{\vec{\mathbf{u}}}^T \widetilde{\mathbf{S}}^T \vec{\mathbf{w}}_\mathrm{f} = \Delta{\vec{\mathbf{u}}}^T \widetilde{\mathbf{S}}^T \left(\vec{\mathbf{w}}_0 + \widetilde{\mathbf{S}}\Delta\vec{\mathbf{u}} \right) = 0 . \tag{10}$$

Equation (7) has been utilized to obtain the last expression in Eq. (10). The non-trivial solution to this equation is:

$$\Delta\vec{\mathbf{u}} = -\left(\widetilde{\mathbf{S}}^T \widetilde{\mathbf{S}} \right)^{-1} \widetilde{\mathbf{S}}^T \vec{\mathbf{w}}_0 = -\widetilde{\mathbf{S}}^+ \vec{\mathbf{w}}_0 = -\widetilde{\mathbf{G}}\vec{\mathbf{w}}_0 , \tag{11}$$

where $\widetilde{\mathbf{G}}$ is the optical control gain matrix, and the superscript "+" denotes the pseudo-inverse of a matrix. It must be pointed out that the actuator commands $\Delta\vec{\mathbf{u}}$ obtained from Eq. (11) are differential values and must be added to the previous values $\vec{\mathbf{u}}_0$ when carrying out the next WFC cycle. The unconstrained least-squares compensator in Eq. (11) is referred to as wavefront control Method 1 in this paper. The $\widetilde{\mathbf{G}}$ is a $N_\mathrm{a} \times N_\mathrm{w}$ matrix and is usually obtained using a singular-value decomposition procedure. The above solution provides the ideal instantaneous control input that would result in a global minimum for the WFE, provided that the sensitivity matrix is exact. The gain matrix $\widetilde{\mathbf{G}}$ has other forms, representing different types of compensators. The one defined in Eq. (11) corresponds to a simple least-squares compensator. Other forms of compensators can be found in Refs. [5-8]. We will introduce two new WF compensators in Section 5 of this paper.

4. METHOD FOR IMPROVING A SENSITIVITY MATRIX

When an adaptive or active optical system utilizes both SD and RB actuators, there are two approaches to perform WFC. In the first approach, one carries out RB actuator WFC first, followed by SD actuator WFC. In this case, two different gain matrices are generated separately from the $\widetilde{\mathbf{S}}_\mathrm{sda}$ and the $\widetilde{\mathbf{S}}_\mathrm{rba}$ defined in Eq. (4). In the second approach, one full WFC cycle is completed in a single-step, using the $\widetilde{\mathbf{S}}$ also defined in Eq. (4). The disadvantage of the first approach is

that the WF needs to be estimated or measured twice to complete a single WFC cycle, requiring longer time to complete one WFC iteration as compared to the second approach.

In both approaches described above, one needs to compute a gain matrix from a measured or simulated sensitivity matrix to perform WFC. To obtain the simulation results to be presented below, we used a detailed and realistic optical model of the HCIT [9]. The 2D OPD map at the exit pupil is obtained by running MACOS (Modeling and Analysis for Controlled Optical Systems) [10] with a given set of parameters. MACOS is a versatile optical modeling tool developed at JPL and used in many flight projects. It allows us to apply a set of actuator commands to the optical model directly, and carry out end-to-end full diffractive propagation analysis to estimate the wavefront at the exit pupil.

As mentioned earlier, sometimes an optical system utilizes mixed types of actuators, such as SD and RB actuators. The responses of different SD actuators can be different, and the RB actuators can also include those that perform RB rotations and those that perform RB translations. Such a situation leads to large differences among the eigen-mode or singular values of the influence functions of different actuators. For example, for the HCIT shown in Fig. 1, we obtained an initial simulated $\widetilde{\mathbf{S}}$ for the 1024 SD actuators of the DM, the tip/tilt (rotation) actuators of the DM and the piston (translation) actuator of the detector. Figure 2 shows the differential optical path difference (OPD) maps, $\widetilde{\mathbf{W}}_i - \widetilde{\mathbf{W}}_{\text{nom}}$, of one SD actuator and the three RB actuators. The SD actuators of the DM utilized on the HCIT have a poke limit of

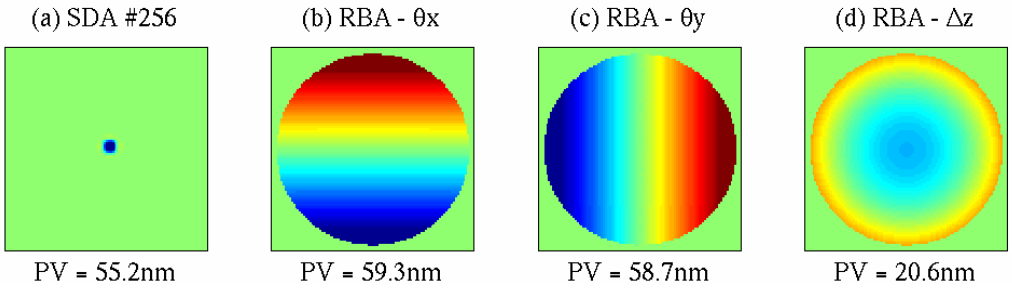

Figure 2. Differential optical path-difference (OPD) $\widetilde{\mathbf{W}}_i - \widetilde{\mathbf{W}}_0$ of 4 different types of actuators. For the SD actuators, only one example is included in Part (a). Parts (b) and (c) correspond to the RB tip/tilt (x- and y-rotations) of the DM, and Part (d) corresponds to the piston of the detector in local coordinate systems. These influence functions are the ones used in all of the numerical examples in this paper. The actuation parameters used are: Stroke $\Delta s = 30$ nm for the SD actuators, $\theta x = \theta y = 1$ μrad for the DM rigid-body actuators, and $\Delta z = 1$ mm for the detector. The same color-map scale is used in all of the OPD maps.

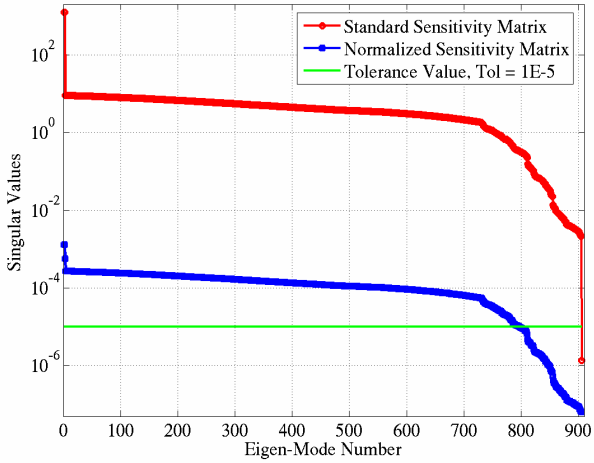

Figure 3. Distributions of singular values of the original $\widetilde{\mathbf{S}}$ (red-curve) as well as the normalized one (blue-curve), $\widetilde{\mathbf{S}}_n$. The green curve represents a pseudo-inverse tolerance value used in one of the numerical examples.

$|u_{sd}| \le 100$nm . Therefore, we used a poke value of $u_{sd} = 30$nm for all of the SD actuators of the DM, $u_\theta = 1$ μrad for the DM tip/tilt actuators, and $u_z = 1$mm for the detector piston actuator in Fig. 2. The same values of actuator commands were used when obtaining the sensitivity matrix used in our numerical examples. The original $\widetilde{\mathbf{S}}_{sda}$ turned out to be a singular matrix. This is caused by the fact the SD actuators located in the 4 corners of the DM are far outside the clear aperture of the system and do not affect the exit pupil WF. Therefore, we first eliminated those SD actuators whose $\vec{\mathbf{w}}_i - \vec{\mathbf{w}}_{nom}$ have a peak-to-valley (PV) values less than 0.1nm. This reduced the number of SD actuators from 1024 to 903 and resulted a new, smaller $\widetilde{\mathbf{S}}_{sda}$. The red-curve in Fig. 3 shows the distribution of the singular values of this new $\widetilde{\mathbf{S}}$ with N_{sda} =903. The condition number (the ratio of the largest singular value to the smallest) of $\widetilde{\mathbf{S}}$ is 9.16×10^8 and the singular-value tolerance as defined in Matlab (see the Help information for "pinv") is 1.95×10^{-9}. That is, the new $\widetilde{\mathbf{S}}$ is no longer singular.

In the example described above, the original $\widetilde{\mathbf{S}}$ becomes singular because the SD actuators located completely outside the clear aperture of the exit pupil do not have an effect on the WF. However, one sometimes encounters a situation, especially in a large space telescope with a fairly complex optical design such as the JWST, where the $\widetilde{\mathbf{S}}$ becomes singular or nearly singular due to the large differences among the influence functions of SD, rotation and translation actuators. One approach to solve this problem is to use a normalized $\vec{\mathbf{s}}_i$, or $\vec{\mathbf{s}}_{ni}$, defined as

$$\vec{\mathbf{s}}_{ni} = \frac{\vec{\mathbf{w}}_i - \vec{\mathbf{w}}_{nom}}{u_i / u_{ni}}, \tag{12}$$

where u_{ni} is the scaling factor. In the following, we use the pair $(\widetilde{\mathbf{S}}_n, \widetilde{\mathbf{G}}_n)$ to denote the corresponding (normalized) sensitivity and gain matrices, respectively. In this case, Eq. (11) becomes as

$$\Delta\vec{\mathbf{U}} = -\widetilde{\mathbf{G}}_n \vec{\mathbf{w}}_0, \qquad \Delta\vec{\mathbf{u}}^T = \left[\Delta U_1 u_{n1} \quad \Delta U_2 u_{n2} \quad \ldots \quad \Delta U_{N_a} u_{nN_a}\right], \tag{13}$$

where $\Delta\vec{\mathbf{U}}$ are the normalized actuator commands. This is one of the new approaches introduced in this paper. This approach is especially useful for beginners in this field. In practice, one can choose the values of u_i for different types of actuators such that the resulting surface figure maps have comparable RMS or PV values, for example, between 100 and 200 nm. In our example shown in Fig. 2, the PV values range from 20 nm to 60 nm for the SD actuators not located near the edges of the exit pupil clear aperture and the other three RB actuators. After choosing the values of u_i in such a way, one can set $u_{ni} = u_i$, that is, the scaling factors of all actuators are equal to their perturbed values. The blue-curve in Fig. 3 shows the distribution of the singular values of $\widetilde{\mathbf{S}}_n$ obtained this way. The condition number of this $\widetilde{\mathbf{S}}_n$ is 1.99×10^4 , and its tolerance is 2.00×10^{-15} . That is, the inversion characteristic of the sensitivity matrix has now improved dramatically by this scaling method.

We now show several WFC examples. Figure 4 shows the exit pupil OPD map of the HCIT before WFC is performed. It is obtained by including the measured figure errors of various optics employed on the HCIT [9], plus some additional low-order Zernike-mode errors introduced by OAP1. Part (a) of Fig. 5 shows the OPD map after a single iteration of WFC using the $\widetilde{\mathbf{G}}_n$ obtained with a tolerance value of *Tol* = 0 or using a simple least-squares compensator. This is equivalent to including all of the eigen-modes in the WFC. The color-scale of this figure is compressed to ± 3nm to make the weak details visible. In reality, there are data points with values outside that range as evidenced by the PV value given as the x-label of the figure. The undesirable, post-control, aberrations in this figure are composed of two parts. The first part includes some "hot" pixels at the edges of the clear aperture and is caused by the saturation of the actuators in those locations. The second part corresponds to the high spatial-frequency components of the OPD map shown in Fig. 4 that fall outside the controllable band of the DM. In a real situation, the error remaining in the wavefront would have other additional components. These include, but not limited to, the error in the wavefront

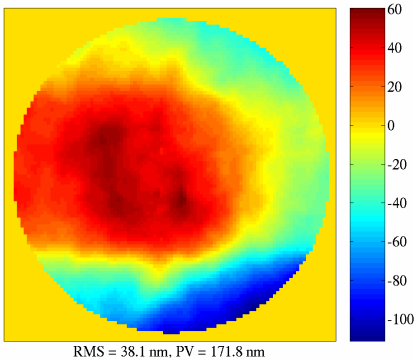

Figure 4. Exit pupil OPD map of the HCIT before WFC. It is obtained by including the measured surface figure maps of the various optics on the HCIT and by introducing some additional low-order Zernike-mode errors into the OAP1. The label underneath the plot displays the RMS and PV values of the OPD map. The color-bar is in nm.

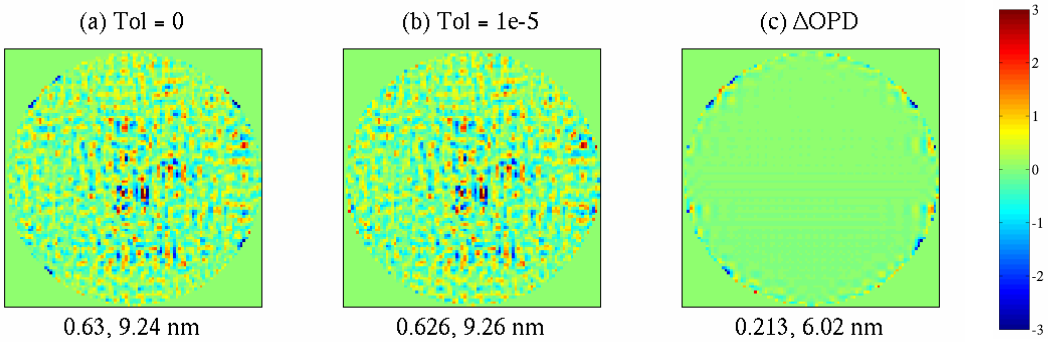

Figure 5. Exit pupil OPD maps of the HCIT after WFC. The gain matrix is obtained from the $\widetilde{\mathbf{S}}_n$ with (a) $Tol = 0$ and (b) Tol =1E-5, respectively. Part (c) shows the difference of the OPD maps shown in Parts (a) and (b). The label underneath each plot displays the RMS and PV values for each plot. The color-bar is in nm.

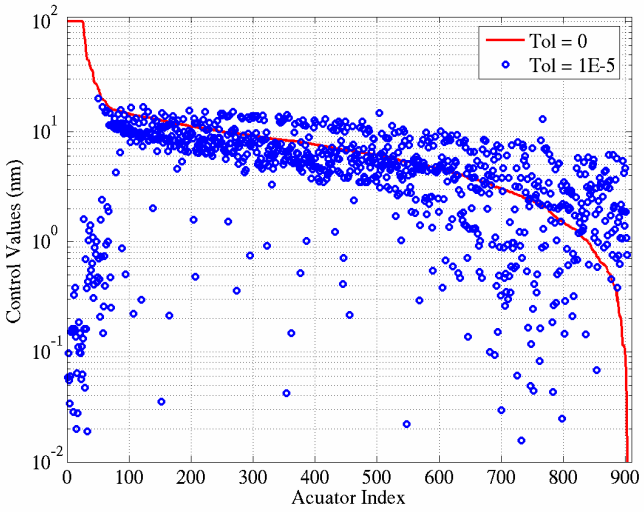

Figure 6. Sorted values of $|u_i|$ used to obtain the results in Fig. 5. The actuator commands obtained with $Tol = 0$ are first sorted in a descending order and plotted as a function of actuator index. The actuator commands obtained with $Tol = 1 \times 10^{-5}$ are also plotted in the same order with blue circles.

estimate $\vec{\mathbf{w}}_0$, actuator error, and the effects of limited spatial resolution in the image plane. For large initial wavefront error the nonlinearity of actuator response to the applied commands also becomes a factor and WFC typically requires more than one iterations to converge.

One well-known approach frequently used in a WFC process is to generate the gain matrix from the corresponding sensitivity matrix with a non-zero tolerance value. We call this WFC approach "a least-squares compensator with a tolerance" and simply refer to it as the wavefront control "Method 2" in this paper. In Matlab, the gain matrix of this approach is obtained as

$$G = pinv(dwdu, Tol)\,. \tag{14}$$

where $dwdu = \widetilde{\mathbf{S}}$. This operation re-distributes the actuation tasks of weak actuators, or actuators whose influences to the WF are much weaker than the normal ones due to some structural difference, structural deficiency or location at the exit pupil, to the neighboring strong actuators and prevents the weak actuators from saturating. For our second example, we used $Tol = 1\times10^{-5}$ to get a new $\widetilde{\mathbf{G}}_{\mathrm{n}}$, and conducted a single-iteration WFC simulation. The residual OPD map of this case is shown in Fig. 5(b), and the difference of the OPD maps in Figs. 5(a) and 5(b) is shown in Fig. 5(c). The RMS and the PV values of the OPD maps in parts (a) and (b) are almost identical. However, we can see from part (c) that the main difference of these two maps are near the edges of exit pupil, and most of the strong residual WF values in part (a) no longer exist in part (b). Figure 6 shows all of the SD actuator commands used to obtain the results in Figs. 5(a) and 5(b), respectively. In this figure, the $|u_i|$ values of all the SD actuators obtained with $Tol = 0$ are sorted in a descending order and plotted as a function of actuator number index in the sorted order using a red-curve. The $|u_i|$ values obtained with $Tol = 1\times10^{-5}$ are also plotted with blue circles in the same order. A total of 25 actuators are saturated and a total of 54 actuators have $|u_i| \geq 20$nm in the case of $Tol = 0$. We found that all of these 54 actuators are located at the edges of the exit pupil. That is, these actuators have weak influences on the WFC process because they are only partially "visible" inside the clear aperture of the exit pupil. Whereas no actuator is saturated and $|u_i| \leq 20$nm for all the actuators in the case where $Tol = 1\times10^{-5}$. Also, many actuators will be forced to have larger stroke values when $Tol = 1\times10^{-5}$ than when $Tol = 0$. For example, note the actuators with indices greater than 600 in Fig. 6.

5. MINIMUM-WAVEFRONT AND OPTIMAL CONTROL COMPENSATOR

In this section, we introduce a new "minimum-wavefront and optimal control compensator". It includes both the WFE and the actuator commands in the cost function to be minimized. This compensator can be used to reduce the overall magnitudes of the actuator commands, and can also be used to control run-away actuator situations. Some control actuations, such as the SD actuators at the edges of a system's clear aperture or a mirror as well as RB rotation and translation actuations, only weakly impact WFE. During a WFC process, these actuators get driven hard to produce a small WF change, usually harder than is desirable and sometimes to the actuation limit. In such a case, some actuators get saturated (reach their actuation limits) and still cannot provide the necessary WF change. This problem can be overcome with a new gain matrix obtained from the following joint cost function:

$$J = \frac{1}{2}\left(\vec{\mathbf{w}}_{\mathrm{f}}{}^{T}\vec{\mathbf{w}}_{\mathrm{f}} + \gamma_{\mathrm{wu}}\vec{\mathbf{u}}^{T}\vec{\mathbf{u}}\right), \tag{15}$$

and by adjusting the γ_{wu} parameter. The control solution is derived in the same way as in Eq. (11). The result is:

$$\Delta\vec{\mathbf{u}} = -\left[\left(\widetilde{\mathbf{S}}^{T}\widetilde{\mathbf{S}}\right)^{-1} + \gamma_{\mathrm{wu}}\widetilde{\mathbf{I}}\right]\widetilde{\mathbf{S}}^{T}\vec{\mathbf{w}}_0 = -\widetilde{\mathbf{G}}\vec{\mathbf{w}}_0\,, \tag{16}$$

where $\widetilde{\mathbf{I}}$ is the identity matrix. This increased versatility comes at the cost of a more complex implementation in the computations, however. We refer to the minimum wavefront and optical control compensator in Eq. (16) as wavefront control Method 3 in this paper.

Here we introduce another, generalized approach to the control that can be quite useful where noise or aliasing is a problem. In this approach, the cost function to be minimized is not the WFE itself, but its spatially-filtered version [8]. This approach may be preferred when a scientific objective calls for a spatially-filtered metric such as encircled energy. Spatial filters can be implemented using a matrix-form Fourier filter. That is,

$$\vec{\mathbf{w}}_{\mathrm{F}} = \widetilde{\mathbf{F}}_{\mathrm{w}} \vec{\mathbf{w}}, \tag{17}$$

Where $\vec{\mathbf{w}}_{\mathrm{F}}$ is the spatially-filtered WF and $\widetilde{\mathbf{F}}_{\mathrm{w}}$ is the spatial filter implemented in a matrix form. A similar filter $\widetilde{\mathbf{F}}_{\mathrm{u}}$ can be added to the actuator command term in Eq. (15). In its most general form, including M_{w} wavefront and M_{a} actuator command spatial filters, the cost function becomes

$$J = \frac{1}{2}\left(\sum_{m=1}^{M_{\mathrm{w}}} \gamma_{\mathrm{w}m} \vec{\mathbf{w}}_{\mathrm{f}}{}^{T} \widetilde{\mathbf{F}}_{\mathrm{w}m}{}^{T} \widetilde{\mathbf{F}}_{\mathrm{w}m} \vec{\mathbf{w}}_{\mathrm{f}} + \sum_{n=1}^{M_{\mathrm{a}}} \gamma_{\mathrm{u}n} \vec{\mathbf{u}}^{T} \widetilde{\mathbf{F}}_{\mathrm{u}n}{}^{T} \widetilde{\mathbf{F}}_{\mathrm{u}n} \vec{\mathbf{u}} \right), \tag{18}$$

from which we obtain the control commands

$$\Delta\vec{\mathbf{u}} = -\left[\sum_{m=1}^{M_{\mathrm{w}}} \gamma_{\mathrm{w}m} \widetilde{\mathbf{S}}^{T} \widetilde{\mathbf{F}}_{\mathrm{w}m}{}^{T} \widetilde{\mathbf{F}}_{\mathrm{w}m} \widetilde{\mathbf{S}} + \sum_{n=1}^{M_{\mathrm{a}}} \gamma_{\mathrm{u}n} \widetilde{\mathbf{F}}_{\mathrm{u}n}{}^{T} \widetilde{\mathbf{F}}_{\mathrm{u}n} \right]^{-1} \left(\sum_{m=1}^{M_{\mathrm{w}}} \gamma_{\mathrm{w}m} \widetilde{\mathbf{S}}^{T} \widetilde{\mathbf{F}}_{\mathrm{w}m}{}^{T} \widetilde{\mathbf{F}}_{\mathrm{w}m} \right) \vec{\mathbf{w}}_{0} = -\widetilde{\mathbf{G}} \vec{\mathbf{w}}_{0}. \tag{19}$$

We call the above approach the "spatially-filtered, minimum wavefront and optimal control compensator".

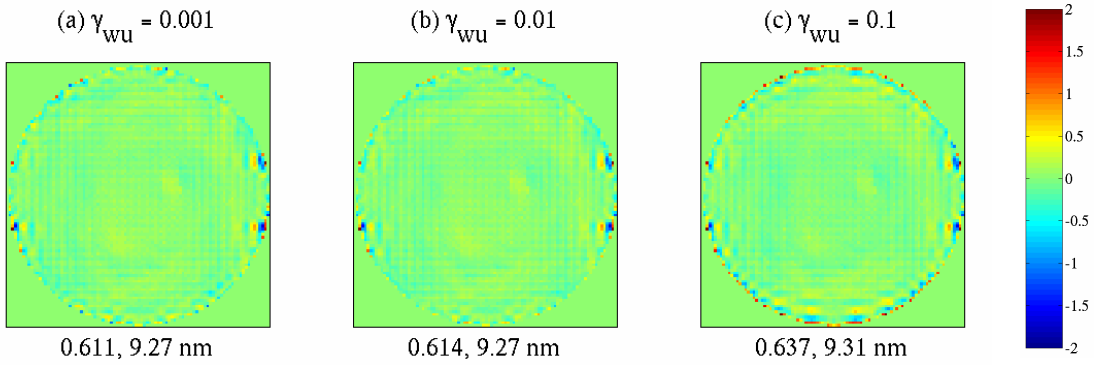

Figure 7. Difference of exit pupil OPD map of the HCIT after WFC obtained with *Tol* =1E-5 minus and OPD maps obtained with γ_{wu} =0.001, 0.01 and 0.1, respectively. The label underneath each plot shows the RMS and the PV values of the after-WFC OPD map obtained using the gain matrix defined in Eq. (16). The color-bar is in nm.

To show the difference of the gain matrices defined in Eqs. (14) and (16), respectively, we carried out some WFC simulations on the optical system in Fig. 1. We used values of 0.001, 0.01 and 0.1 for γ_{wu}, and compared the OPD maps after WFC with that obtained with $Tol = 1\times10^{-5}$, see Fig. 5(b). Figures 7(a)-7(c) show the difference of the OPD map in Fig. 5(b) and those obtained with γ_{wu} =0.001, 0.01 and 0.1, respectively. Just like in the case of Fig. 5(b), the WFC was carried out for only one iteration in the current case. As seen from Figs. 7, the OPD maps after WFC obtained from the above two approaches are mainly different at the edges of the resulted OPD maps; the WFE values at the edges get less suppressed with increased γ_{wu} as compared the case of $Tol = 1\times10^{-5}$. We sorted the control values corresponding to $Tol = 1\times10^{-5}$ in descending order, and plotted them as well as the control values corresponding to γ_{wu} =0.001 in the same order in Fig. 8(a). In Fig. 8(b), we presented the histograms of the control values obtained with $Tol = 1\times10^{-5}$ as well as with the three different values of γ_{wu}. These figures show that the Method 3 compensator

extends the range of $\Delta\vec{\mathbf{u}}$ as compared to Method 2. Also, Fig. 8(b) shows that increasing the value of γ_{wu} reduces the number actuators with large control values, as expected.

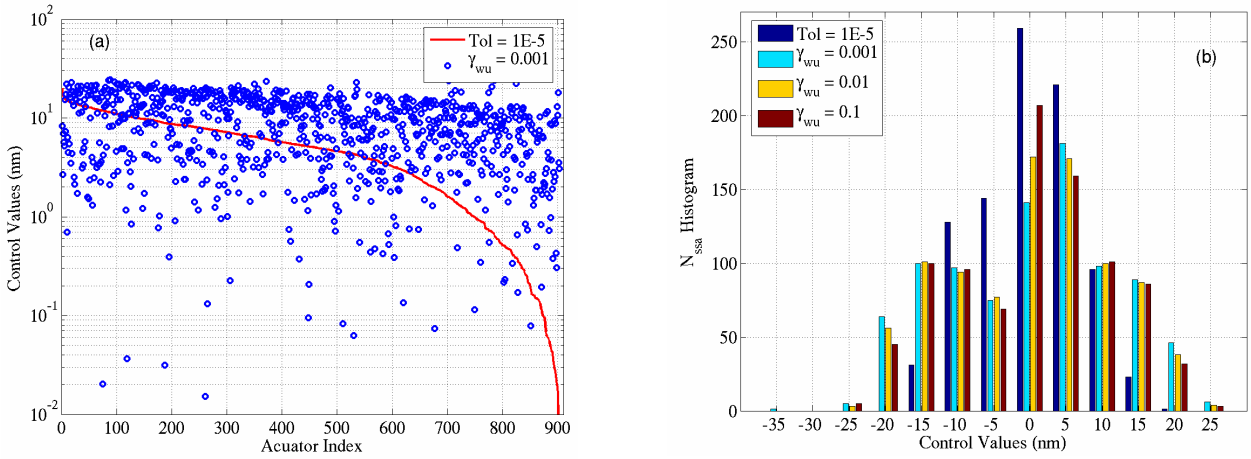

Figure 8. Distribution of control values $|\Delta\vec{\mathbf{u}}|$ obtained in a single-cycle WFC simulation. (a) The control values of the case *Tol* = 1E-5 are sorted in a descending order and plotted with a red-curve. The $|\Delta\vec{\mathbf{u}}|$ of the case $\gamma_{wu} = 0.001$ are also plotted with blue-circles in the same order. (b) Histograms of the control values obtained with two different compensators. For the case of Eq. (16), the values of $\Delta\vec{\mathbf{u}}$ corresponding to three different γ_{wu} –values are included. All control values are for SD actuators only; the control values of the RB actuators are not included in these figures.

6. CONCLUSION

We have introduced a new method for preventing the sensitivity matrix of a large space telescope from becoming singular. In this method, the re-conditioning of the sensitivity matrix into a well-behaved one in terms of invertibility is accomplished by using a set of appropriately selected scaling factors for all actuator commands. This method is very useful when the exit pupil wavefront of the telescope is controlled with both surface-deforming and rigid-body actuators that differ greatly from one another in their influences on the wavefront. We have explained this new approach with some numerical examples obtained through modeling and simulations conducted on the optical model of the High-Contrast Imaging Testbed (HCIT) at JPL.

We have also described several commonly used or available wavefront compensators or control methods. These methods include:

Method 1: Simple least-squares compensator, Eq. (11)
Method 2: Simple least-squares compensator with a tolerance, Eq. (14)
Method 3: Minimum wavefront and optical control compensator, Eq. (16)
Method 4: Generalized, spatially-filtered minimum wavefront and optical control compensator, Eq. (19)

Among them, Methods 3 and 4 have been reported for the first time in this paper. In these two methods, the WFS signals as well as the actuator commands are included in the feedback loop. The actuator command terms provide direct observability of actuator modes that are not observable in the WFS signals, thus eliminating susceptibility to "waffle" and other problematic modes. We have shown using some HCIT simulation results that Method 3 is comparable to Method 2 in terms of controlling run-away actuator situations or preventing the "weak" actuators from getting saturated during a wavefront control operation. We have used these two methods successfully in several different experiments and projects. They have been found to be useful in situations with uncertain parameters, nonlinear actuators, influence function errors, and/or high noise. They may have poorer predicted performance in linear models of the mirror control problem, yet yield better overall performance, because they are less dependent on the absolute accuracy of the control models. They avoid problems where a controller will drive actuators in opposition to create a small theoretical

beneficial effect -- a small difference of large numbers -- only to find that the errors in the large numbers create a larger error than the expected small benefit. We expect that both the sensitivity matrix normalization method and the minimum wavefront and optimal control compensator presented in this paper will play important roles in large space telescopes.

REFERENCES

1. Daniel S. Acton, Paul D. Atcheson, Mick Cermak, Lana K. Kingsbury, Fang Shi and David C. Redding, "James Webb Space Telescope wavefront sensing and control algorithms," Proc. SPIE, **5487**, 887, 2004.
2. D. Redding, S. Basinger, G. Brack, and R. Dekany, "Adaptive optics reconstruction utilizing super-sampled deformable mirror influence functions," Proc. SPIE, **3353**, 543, 1998.
3. Andrew E. Lowman, John T. Trauger, Brian Gordon, Joseph J. Green, Dwight Moody, Albert F. Niessner, and Fang Shi, "High-contrast imaging testbed for the Terrestrial Planet Finder coronagraph," Proc. SPIE, **5487**, 1246, 2004.
4. John T. Trauger, Chris Burrows, Brian Gordon, Joseph J. Green, Andrew E. Lowman, Dwight Moody, Albert F. Niessner, Fang Shi, and Daniel Wilson, "Coronagraph contrast demonstrations with the high-contrast imaging testbed," Proc. SPIE, **5487**, 1330, 2004.
5. W. Wild, "Innovative wavefront estimators for zonal adaptive optics," Proc. SPIE, **3126**, 278, 1997.
6. D. Redding, S. Basinger, A. E. Lowman, and A. Kissil, "Wavefront sensing and control for a next generation space telescope," Proc. SPIE, **3356**, 758, 1998.
7. D. Redding, S. Basinger, G. Brack, and R. Dekany, "Adaptive optics reconstruction utilizing super-sampled deformable mirror influence functions," Proc. SPIE, **3356**, 543, 1998.
8. D. Redding, F. Shi, S. Basinger, D. Cohen, J. J. Green, A. E. Lowman, and C. M. Ohara, "Wavefront sensing and control for large space optics," IEEEAC Proc. Vol. **4-1729**, 1-16, 2003.
9. Erkin Sidick, Fang Shi, Scott Basinger, Dwight Moody, Andrew E. Lowman, Andreas C. Kuhnert, and John T. Trauger, "Performance of TPF's High-Contrast Imaging Testbed: Modeling and simulations, "Proc. SPIE, **6265**, 62653L, 2006.
10. *Modeling and Analysis for Controlled Optical Systems (MACOS) User's Manual*, Jet Propulsion Laboratory, California Institute of Technology, Pasadena, CA.